Mechanism of Nucleation Pathway Selection in Binary Lennard-Jones Solution: A Combined Study of Molecular Dynamics Simulation and Free Energy Analysis

Yuya Iida, Tatsumasa Hiratsuka, Minoru T. Miyahara, and Satoshi Watanabe*

Department of Chemical Engineering, Kyoto University, Katsura, Nishikyo, Kyoto 615-8510, Japan

KEYWORDS: nucleation, molecular dynamics, nucleation pathway, free energy analysis, Lennard-Jones system

ABSTRACT: The nucleation process, which is the initial step in particle synthesis, determines the properties of the resultant particles. Although recent studies have observed various nucleation pathways, the physical factors that determine these pathways have not been fully elucidated. Herein, we conducted molecular dynamics simulations in a binary Lennard-Jones system as a model solution and found that the nucleation pathway can be classified into four types depending on microscopic interactions. The key parameters are (1) the strength of the solute-solute interaction, and (2) the difference between the strengths of the like-pair and unlike-pair interactions. The increment of the former alters the nucleation mechanism from a two-step to a one-step pathway, whereas that of the latter causes quick assembly of solutes. Moreover, we developed a thermodynamic model based on the formation of core-shell nuclei to calculate the free energy landscapes. Our model successfully described the pathway observed in the simulations and demonstrated that the two parameters, (1) and (2), define the degree of supercooling and supersaturation, respectively. Thus, our model interpreted the microscopic insights from a macroscopic point of view. Because the only inputs required for our model are the interaction parameters, our model can *a priori* predict the nucleation pathway.

Introduction

Particles are one of the most important forms of material involved in industrial processes. Most industrial products form particles as precursors or as final products in production processes. The quality of the products depends on the properties of the relevant particles, including their sizes, shapes, and crystal polymorphs. For instance, nanoparticles of semiconductors (quantum dots) require a sharp size distribution within nanometer scale for their peculiar optical and electronic properties.[1] Another example is the pharmaceuticals that must have specific crystal polymorphs for demonstrating the targeted drug effects.[2] These geometric characteristics of particles are determined in the nucleation process, which is the initial step of particle formation. Therefore, it is essential to control the nucleation process to obtain desired product properties. However, the nucleation process has been a great mystery, possibly because of the challenge of direct observation and experimental detection.

From a thermodynamic point of view, nucleation is an activation process to transition from a metastable homogeneous phase, such as saturated vapors, melts, and solutions, to a new phase with the global minimum of the free energy. The most popular theoretical framework for describing nucleation processes is the classical nucleation theory (CNT), which was originally proposed by Gibbs[3] and thereafter followed by refinements.[4–6] In the CNT framework, one-step nucleation is assumed, in which a nucleus has an identical structure to the bulk of the new phase. Based on the one-step pathway assumption, the CNT demonstrates a free energy profile of the nucleation process along the nucleus size as a reaction coordinate. This free energy profile is determined by the balance between the stabilization arising because of the formation of a new stable phase and the energy penalty owing to interface formation. The free energy profiles predicted by the CNT provide a qualitative understanding of nucleation. However, a limitation with CNT is that it fails in quantitative prediction as the predicted nucleation rates often vary from those obtained from experiments and simulations by orders of magnitude.[7–10]

In the last few decades, numerous studies have revealed that the one-step pathway assumption in CNT is not always valid, and this could be the source of failure in making the quantitative description. A wide variety of pathways have been accordingly proposed and demonstrated, including a multi-step pathway leading to the new stable phase via one or more intermediate states,[11] aggregation of precursors called prenucleation clusters,[12,13] and oriented attachment.[14] In particular, the "two-step pathway," in which the formation of disordered liquid-cluster precedes crystallization, has been demonstrated as a highly general pathway observed in a wide range of systems like proteins,[15] colloidal particles,[16] small organic molecules,[17] and electrolytes.[18,19] Furthermore, the

nucleation process can vary from a CNT-like one-step pathway to a two-step one depending on the solute concentration and solvent.[18,20] Therefore, elucidating the key physical factors that determine the nucleation pathway has become a crucial issue to understand and control the nucleation processes.

A practical and effective approach to identify and understand the key factors is the modeling of molecules by simplifying molecular shapes and interactions. This includes lattice models,[21–23] hard spheres,[24,25] and Lennard-Jones (LJ) molecules.[26–28] Simple modeling does not adhere to specific properties of molecules, but instead extracts general properties to reveal certain intrinsic physical factors governing the nucleation phenomena. For example, simulation studies of lattice and LJ systems have demonstrated that the one-step pathway appears under strong anisotropic interactions and low temperatures.[23,26,27] Other simulations of coarse-grained protein molecules in solution have shown the importance of short-range and non-anisotropic intermolecular interactions in the two-step pathway.[29,30] For a more quantitative understanding, combining the simulations described above with a thermodynamic model[31,32] is also a powerful approach. Eaton *et al*.[22] calculated the free energy profiles of the nucleation processes in a lattice model system using a "core-shell CNT" model. In this thermodynamic model, two-step nucleation was represented by assuming the formation of a nucleus with a core-shell structure in which a metastable phase shell surrounded the stable phase core. The free energy profiles calculated from the core-shell CNT model quantitatively agreed with those calculated directly from the simulations using umbrella sampling. The core-shell CNT model fairly reproduces the nucleation characteristics of the two-step pathway and clarifies the effects of the interaction factors through the free energy profiles. Recently, the core-shell CNT model was utilized in a more complex system. Bulutoglu *et al*. successfully applied the core-shell CNT model to a realistic molecular solution system (NaCl solution) to explain the pathway variation in terms of the free energy.[33] However, their methodology relied on parameter fitting of free energy profiles obtained from simulations to calculate the chemical potential and interfacial energy. Because numerous factors generally affect nucleation behaviors in systems consisting of multiple molecular species,[34–36] predicting pathways based solely on the physical properties of the constituent molecules remains a challenge.

To elucidate the key factors governing the nucleation pathway and to enable the pathway prediction, we performed molecular dynamics simulations in a binary LJ system under various interaction parameter conditions. We developed an extended core-shell CNT model applicable to solution systems by considering the system as a regular solution. The free energy profiles calculated from the core-shell CNT model based on the interaction parameters were in good agreement with the pathways observed in the simulations. We successfully demonstrated that the core-shell CNT model predicts the nucleation pathways in molecular solution systems with explicit solvents. Furthermore, we discussed the physical meaning of each parameter in our model and found that the supersaturation of the solution phase and supercooling of the metastable phase are the key macroscopic factors in determining the nucleation pathway. Notably, we clarified that these macroscopic key factors are the functions of the interaction parameters, which opens up the possibility of predicting and controlling the nucleation pathways through microscopic interaction parameters.

Methods

Details of the molecular dynamics simulation

We performed molecular dynamics simulations in a binary LJ system composed of solute molecules A and solvent molecules B. The two-body interaction ϕ_{ij} is expressed as follows:

$$\phi_{ij} = 4\varepsilon\left\{\left(\frac{\sigma}{r_{ij}}\right)^{12} - \left(\frac{\sigma}{r_{ij}}\right)^{6}\right\}, \quad (1)$$

where r_{ij} is the distance between molecules i and j, σ and ε are LJ parameters representing the effective molecular size and strength of the interaction, respectively. The parameters of the MD simulations are summarized in Table 1. The parameters were selected based on the reported phase diagram[37] so that the temperature and pressure (density) conditions ensure the equilibrium state to form the liquid phase of the solvent molecules and the solid phase of the solute molecules. To systematically investigate the effects of interaction strength on the nucleation behavior, we varied normalized interaction strength $\varepsilon^* = \varepsilon/kT$. We set the molecular size σ to be identical for solutes and solvents. Molecular dynamics simulations were conducted using the open-source simulator GROMACS (version 2019.4). All the simulation runs were performed in the *NPT* ensemble at 0.77 kbar by using the velocity rescaling thermostat[38] and the Parrinello–Rahman barostat[39] as implemented in GROMACS. The temperature was set as 180 K unless otherwise stated. Periodic boundary conditions were applied in all three directions of a cubic cell. The time step was set to 2 fs. The potential was cut and shifted at $4\sigma_{AA}$. Because nucleation is a stochastic process, simulations were performed with multiple initial solution configurations for a single condition. The initial configuration of the solute and solvent molecules in the solution was created using the following procedure: (1) Solute and solvent molecules were randomly placed in the cubic cell with the dimensions of 15.5 nm × 15.5 nm ×15.5 nm (GROMACS

Table 1. Parameters of MD simulations

Parameter			
LJ parameter	$\varepsilon^* = \varepsilon/kT$ [−]	σ [Å]	
solute-solute	$\varepsilon^*_{AA} = \varepsilon_{AA}/kT$: 2.0, 2.67	σ_{AA}:	3.0
solvent-solvent	$\varepsilon^*_{BB} = \varepsilon_{BB}/kT$: 1.0 − 1.34	σ_{BB}:	3.0
solute-solvent	$\varepsilon^*_{AB} = \varepsilon_{AB}/kT$: 0.83 − 1.70	σ_{AB}:	3.0
# of molecules [−]			
Solute	1500		
Solvent	24000		
Molecular weight [g/mol]	5		

command "insert-molecules"). (2) Under a set of parameters of $\varepsilon^*_{AA} = \varepsilon^*_{BB} = \varepsilon^*_{AB} = 1.2$, in which the system takes liquid phase at equilibrium, the system was relaxed by a 30-ps run with a time step of 0.05 fs. (3) The solution was then equilibrated through a 60-ps run with a time step of 2 fs. (4) Finally, under the condition of a desired set of interaction parameters and temperature, the system was relaxed by a 15-ps run with a time step of 0.5 fs.

Identification of liquid cluster and crystals

To detect the nucleation behavior in which solute molecules spontaneously form assembled structures from a solution state, we calculated coordination numbers and bond-orientational order parameters of solute molecules to classify an assembled structure as a liquid cluster or a crystal, and traced the number of solute molecules in the largest assembled structure, n_L, and that in the largest crystal, n_C, based on the following procedure proposed by Tribello *et al.*[40] Following analyses were all conducted using PLUMED (version 2.5.4) software packages. The coordination number of molecule *i*, c_i, was calculated as the number of molecules within a threshold distance from the center of molecule *i*.

$$c_i = \sum_j f(r_{ij}). \qquad (2)$$

$f(r_{ij})$ is a smooth step function as defined by the following equation:

$$f(r_{ij}) = \begin{cases} 1 & (r_{ij} \le r_1) \\ (y-1)^2(1+2y) & (r_1 < r_{ij} \le r_2) \\ 0 & (r_{ij} > r_2) \end{cases} \qquad (3)$$

with $$y = \frac{r_{ij} - r_1}{r_2 - r_1},$$

where $r_{ij} \le r_1$ is fully coordinated, $r_1 < r_{ij} \le r_2$ is partially coordinated, and $r_{ij} > r_2$ is not coordinated. For solute molecules with a coordination number c_i greater than or equal to a threshold c_0, we conducted an analysis based on graph theory to obtain the number of constituent solute molecules in a liquid cluster. In the present analysis, we set r_1 and r_2 as $2^{1/6}\sigma_{AA}$, at which the interaction potential between solute molecules has the minimum, and $1.3\sigma_{AA}$, respectively, and c_0 as 3. We used the Steinhardt bond-orientational parameter $Q_6^{(i)}$ to evaluate the degree of orientational order of the assembled structure. First, we calculated the following vector $\boldsymbol{q}_6^{(i)}$ for each molecule *i*:

$$\boldsymbol{q}_6^{(i)} = \left[q_{6,-6}^{(i)}, q_{6,-5}^{(i)}, \cdots, q_{6,0}^{(i)}, q_{6,1}^{(i)}, q_{6,2}^{(i)}, \cdots, q_{6,6}^{(i)}\right], \qquad (4)$$

$$\text{where } q_{6,m}^{(i)} = \frac{\sum_{j \ne i} f(r_{ij}) Y_{6m}(\boldsymbol{r}_{ij})}{\sum_{j \ne i} f(r_{ij})}.$$

Herein, $Y_{6m}(\boldsymbol{r}_{ij})$ are the 6th spherical harmonics. We then computed $Q_6^{(i)}$ as follows:

$$Q_6^{(i)} = \frac{\sum_{j \ne i} f(r_{ij}) \boldsymbol{q}_6^{(i)} \cdot \boldsymbol{q}_6^{(j)}}{\sum_{j \ne i} f(r_{ij})}. \qquad (5)$$

When the crystallinity is high, molecules *i* and *j* have similar orientations, $\boldsymbol{q}_6^{(i)}$ and $\boldsymbol{q}_6^{(j)}$ have identical directions so that their inner product $\boldsymbol{q}_6^{(i)} \cdot \boldsymbol{q}_6^{(j)}$ and consequently $Q_6^{(i)}$ becomes large. In the present study, we assumed solute molecules with $Q_6^{(i)} \ge 0.5$ as crystalline molecules and otherwise as components of a liquid cluster. For the crystalline molecules, we conducted the same analysis as above, based on graph theory, to obtain the number of constituent solute molecules in a crystal domain.

Results and discussion

Pathway selection in binary LJ solutions

We first conducted a simulation under $(\varepsilon^*_{AA}, \varepsilon^*_{BB}, \varepsilon^*_{AB}) = (2.0, 1.34, 1.34)$ as a typical condition. Figure 1 shows snapshots of the simulation, and Fig. 2a shows the corresponding time course of the number of solute molecules in the largest assembled structure, n_L, and the largest crystal, n_C. In the initial solution state (Fig. 1(I)), n_L and n_C are approximately zero, because there are no assembled structures. After induction time t_L, n_L rapidly increases to approximately 800, indicating the formation of a single solute-rich liquid cluster, as shown in Fig. 1(II). The liquid cluster crystallizes (Fig. 1(III)) after another induction time, t_C, accompanied by a steep increase in n_C. Thus, the system with the typical condition exhibits two-step nucleation with induction times for both liquid-cluster formation and crystallization. We then investigated the effects of solute-related interactions on the nucleation behavior by varying the solute-solute and solute-solvent interactions, ε^*_{AA} and ε^*_{AB}, from those under typical condition. We observed four different types of nucleation behavior, as summarized in Fig. 2, including the two-step nucleation under typical condition (Fig. 2a). In the case of larger values of ε^*_{AA} and ε^*_{AB} (Fig. 2b), n_L and n_C increase almost simultaneously, indicating that nucleation occurs along a one-step pathway. When only ε^*_{AB} is decreased from the typical condition, the solutes assemble without an induction time ($t_L \approx 0$), whereas crystallization occurs with a certain induction time at $n_L \approx 1400$ (Fig. 2c). The stair-like increase in n_L corresponds to the formation of multiple liquid clusters and their subsequent coalescence. When only ε^*_{AA} is increased, multiple crystals rapidly form in a one-step pathway without an induction time (Fig. 2d). A similar trend was also observed when the solvent-solvent interaction strength ε^*_{BB} was varied as shown in Fig. 3 which shows the average induction time for liquid cluster formation, τ_L, (See supplemental material), and the mean n_L at the crystallization for various parameter sets calculated from

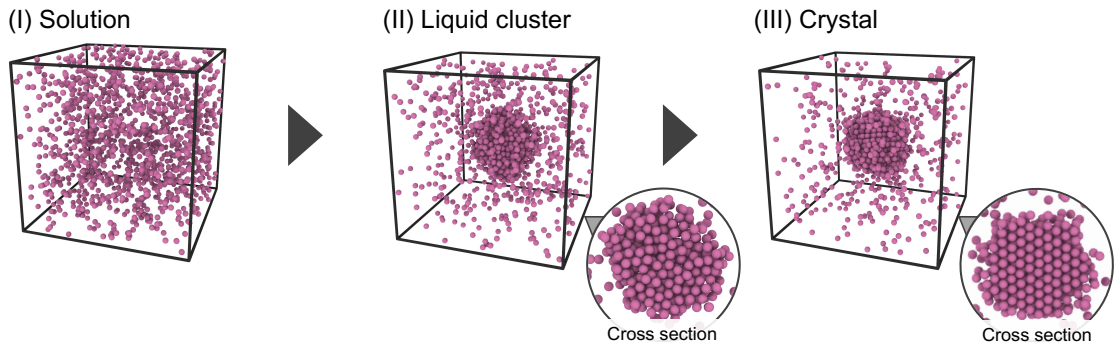

Fig. 1. Snapshots from MD simulation for a parameter set of $(\varepsilon^*_{AA}, \varepsilon^*_{BB}, \varepsilon^*_{AB}) = (2.0, 1.34, 1.34)$, in which only solute molecules are shown for clarity. The lower right insets of states (II) and (III) are the cross-sectional views of the assembled structures.

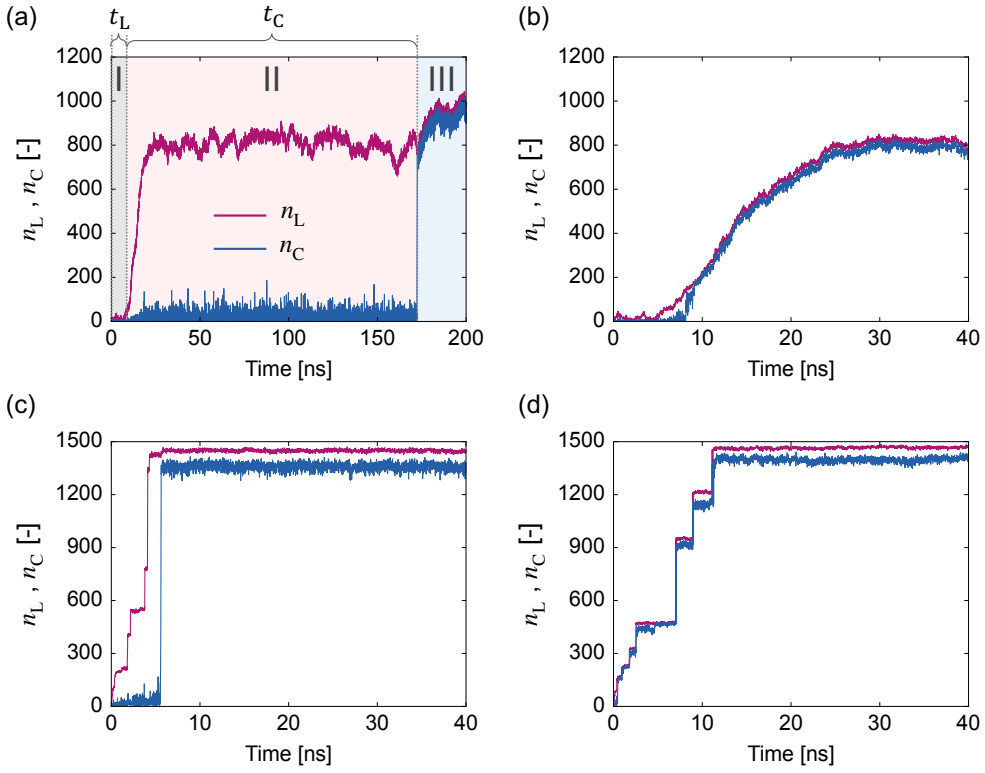

Fig. 2. Time courses of n_L and n_C for four parameter sets of (a) $(\varepsilon^*_{AA}, \varepsilon^*_{BB}, \varepsilon^*_{AB}) = (2.0, 1.34, 1.34)$, $\Delta\varepsilon^* = 0.67$, (b) $(\varepsilon^*_{AA}, \varepsilon^*_{BB}, \varepsilon^*_{AB}) = (2.67, 1.34, 1.70)$, $\Delta\varepsilon^* = 0.60$, (c) $(\varepsilon^*_{AA}, \varepsilon^*_{BB}, \varepsilon^*_{AB}) = (2.0, 1.34, 1.0)$, $\Delta\varepsilon^* = 1.34$, and (d) $(\varepsilon^*_{AA}, \varepsilon^*_{BB}, \varepsilon^*_{AB}) = (2.67, 1.34, 1.34)$, $\Delta\varepsilon^* = 1.34$. In figure (a), time zones I, II, and III correspond to solution state (I), liquid cluster (II), and crystal (III) of Fig. 1, respectively.

multiple simulation runs. Figure 3 clearly demonstrates that the nucleation behavior can be classified into four types by the induction times for liquid cluster formation and the cluster size at crystallization for different combinations of the interaction parameters, ε^*_{AA}, ε^*_{BB}, and ε^*_{AB}. These nucleation behaviors can be qualitatively accounted for by considering the contributions of ε^*_{AA}, ε^*_{BB}, and ε^*_{AB} to the formation and crystallization of liquid clusters. Generally, large values of ε^*_{AA} and ε^*_{BB} favor a phase-separated state between the species A and B because of the strong like-pair interactions, whereas a large value of ε^*_{AB} facilitates the mixing of A and B owing to the strong unlike-pair interactions. Given the assumption that the phase separation of mixtures A and B breaks two A-B interactions and replaces them with one A–A and one B-B interaction, the driving force for liquid cluster formation should be represented by $\Delta\varepsilon^* = \varepsilon^*_{AA} + \varepsilon^*_{BB} - 2\varepsilon^*_{AB}$ For crystallization, the driving force should be primarily characterized by the solute-solute interaction ε^*_{AA}, because liquid clusters are solute-rich. The results shown in Figs. 2 and 3 confirm this trend because a higher value of $\Delta\varepsilon^*$ results in the quick assembly of solutes without any induction time (Figs. 2c, 2d, and the open diamonds and circles in Fig. 3), and a higher value of ε^*_{AA} induces instantaneous crystallization to yield one-step pathways (Figs. 2b, 2d, and the open and closed diamonds in Fig. 3). These results demonstrate that the determinants of the nucleation behavior are $\Delta\varepsilon^*$ and ε^*_{AA}.

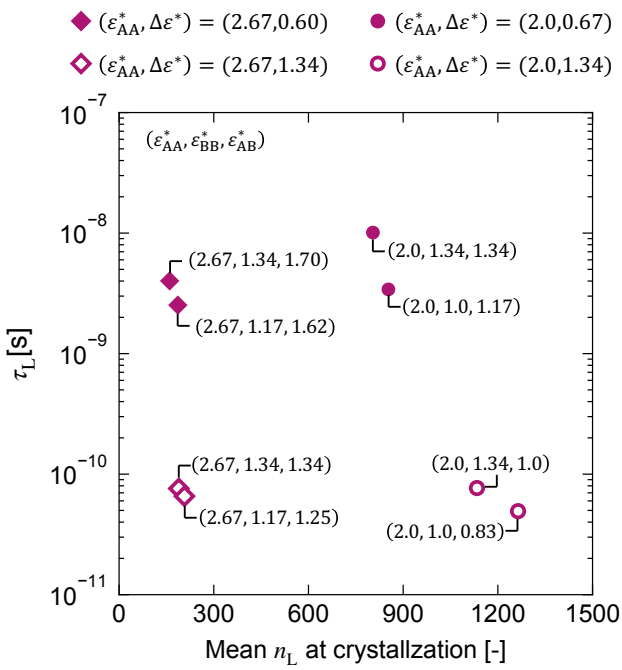

Fig. 3. Average induction time for liquid cluster formation τ_L and mean cluster size n_L at crystallization for various parameter sets. The simulations for the parameter sets of $(\varepsilon^*_{AA}, \varepsilon^*_{BB}, \varepsilon^*_{AB}) = (2.0, 1.0, 1.17)$ and $(2.0, 1.0, 0.83)$ were conducted at 240 K.

Theory: Core-shell CNT model

To explain the nucleation behavior in our MD simulation more quantitatively, we developed a thermodynamic model by extending the core-shell CNT model proposed by Kashchiev[32] to a solution system. We considered the finite size effect to compare with the MD simulations. As shown in Fig. 4, let us consider the formation process of a nucleus, which is composed of a pure solute crystal core surrounded by a solute-rich shell with a composition $x_{is}(i = \mathrm{A}, \mathrm{B})$, from a solution phase of an initial composition $x_{i0} = N_i/(N_\mathrm{A} + N_\mathrm{B})$, where N_A and N_B indicate the number of solutes and solvents, respectively. We defined the number of solute and solvent molecules in the nucleus as n_L, and n_B, respectively, and that of the solute molecules in the crystal core as n_C. The shell consists of $n_\mathrm{L} - n_\mathrm{C}$ solutes and n_B solvents. Using the shell composition x_{is}, we obtain n_B as follows:

$$n_\mathrm{B} = (n_\mathrm{L} - n_\mathrm{C})\frac{x_\mathrm{Bs}}{x_\mathrm{As}}. \tag{6}$$

Because of the finite system size, nucleation involves a compositional change in the solution phase from x_{i0} to x_{ia}. The x_{ia} is given by

$$x_\mathrm{Aa} = \frac{N_\mathrm{A} - n_\mathrm{L}}{N_\mathrm{A} + N_\mathrm{B} - n_\mathrm{L} - n_\mathrm{B}}, x_\mathrm{Ba} = \frac{N_\mathrm{B} - n_\mathrm{B}}{N_\mathrm{A} + N_\mathrm{B} - n_\mathrm{L} - n_\mathrm{B}}. \tag{7}$$

The free energy change due to the formation of a core-shell nucleus is divided into a volume term ΔG_V, which is the stabilization term owing to the formation of a new stable phase, and an interface term ΔG_S, the energy penalty term because of interface formation:

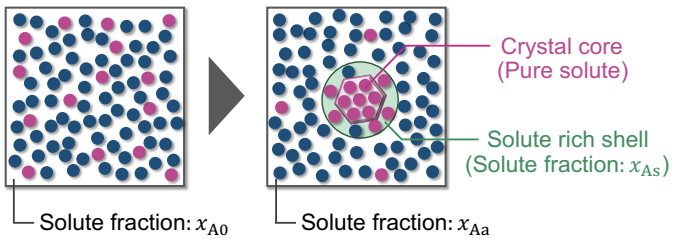

Fig. 4. Schematic of the proposed model.

$$\Delta G = \Delta G_V + \Delta G_S. \tag{8}$$

The volume term, ΔG_V is calculated based on the chemical potential. The free energy of the initial solution G_0 is given by:

$$G_0 = N_\mathrm{A}\mu_\mathrm{A}(x_\mathrm{A0}) + N_\mathrm{B}\mu_\mathrm{B}(x_\mathrm{B0}), \tag{9}$$

where $\mu_i(x_i)$ is the chemical potential of component i in a solution of composition x_i. After nucleation, the system contains three phases: core, shell, and solution. Their contribution to the free energy of the system G_a is expressed by the following equation:

$$\begin{aligned} G_\mathrm{a} &= n_\mathrm{C}\mu^*_\mathrm{A,C} \\ &+(n_\mathrm{L} - n_\mathrm{C})\mu_\mathrm{A}(x_\mathrm{As}) + n_\mathrm{B}\mu_\mathrm{B}(x_\mathrm{Bs}) \\ &+(N_\mathrm{A} - n_\mathrm{L})\mu_\mathrm{A}(x_\mathrm{Aa}) + (N_\mathrm{B} - n_\mathrm{B})\mu_\mathrm{B}(x_\mathrm{Ba}), \end{aligned} \tag{10}$$

where $\mu^*_\mathrm{A,C}$ is the chemical potential of the crystal of the pure solute. Considering the difference in Eqs. (9) and (10), we obtain the following general expression for ΔG_V:

$$\begin{aligned} \Delta G_V &= n_\mathrm{C}\{\mu^*_\mathrm{A,C} - \mu_\mathrm{A}(x_\mathrm{A0})\} \\ &+(n_\mathrm{L} - n_\mathrm{C})\{\mu_\mathrm{A}(x_\mathrm{As}) - \mu_\mathrm{A}(x_\mathrm{A0})\} \\ &+n_\mathrm{B}\{\mu_\mathrm{B}(x_\mathrm{Bs}) - \mu_\mathrm{B}(x_\mathrm{B0})\} \\ &+(N_\mathrm{A} - n_\mathrm{L})\{\mu_\mathrm{A}(x_\mathrm{Aa}) - \mu_\mathrm{A}(x_\mathrm{A0})\} \\ &+(N_\mathrm{B} - n_\mathrm{B})\{\mu_\mathrm{B}(x_\mathrm{Ba}) - \mu_\mathrm{B}(x_\mathrm{B0})\}. \end{aligned} \tag{11}$$

The interface term ΔG_S includes the contribution from the two interfaces (solution/shell and shell/core) and is expressed as follows:

$$\Delta G_S = \gamma_\mathrm{L} S_\mathrm{L} + \gamma_\mathrm{C} S_\mathrm{C} + \Psi, \tag{12}$$

where $\gamma_\mathrm{L}$and γ_C are the interfacial tensions of solution/shell and shell/core interfaces, respectively, S_L and S_C are the interface areas of solution/shell and shell/core interfaces, respectively, and Ψ is the interaction between the two interfaces owing to their proximity. By assuming that both the core and shell are spherical and the volume change due to the mixing of solutes and solvents is negligible, S_L and S_C are represented by n_L and n_C, and the occupied volumes of solute molecules in the solution and crystal are v_L and v_C, respectively, we arrive at the following equation of ΔG_S:

$$\begin{aligned} \Delta G_S = \gamma_\mathrm{L} a_\mathrm{L}^{\frac{2}{3}}\left\{(n_\mathrm{L} - n_\mathrm{C})\left(1 + \frac{r x_\mathrm{Bs}}{x_\mathrm{As}}\right) + n_\mathrm{C}\frac{v_\mathrm{C}}{v_\mathrm{L}}\right\}^{\frac{2}{3}} \\ + \gamma_\mathrm{C} a_\mathrm{C}^{\frac{2}{3}} n_\mathrm{C}^{\frac{2}{3}} + \Psi, \end{aligned} \tag{13}$$

where $a_\mathrm{L} = 6\sqrt{\pi}v_\mathrm{L}$, $a_\mathrm{C} = 6\sqrt{\pi}v_\mathrm{C}$, and r is the volume ratio of the solute to solvent molecule. Owing to the simplicity of the binary LJ system, the free energy changes, ΔG_V and ΔG_S, were expressed as the functions of the molecular properties (ε and

σ) and operating conditions (the number of molecules, temperature, and concentration), the details of which are as follows. By considering a binary LJ system as a regular solution, the chemical potential and the shell composition $x_{i,s}$ can be derived as the functions of ε and σ based on the change in the mixing free energy of the solute and the solvent (See supplementary material: detailed derivation and the validation of our model is available). By substituting the chemical potentials in Eq. (S-12), (S-13), and (S-14) into Eq. (11), the volume term ΔG_V is given by:

$$\begin{aligned}\Delta G_V &= n_{\mathrm{C}}kT\left[-Z_{\mathrm{m}}\varepsilon^*_{\mathrm{AA}}\left(\frac{T_{\mathrm{mb}}-T}{T_{\mathrm{mb}}}\right)-\ln x_{\mathrm{Aa}}-\beta{\phi_{\mathrm{Ba}}}^2\right]\\ &+(n_{\mathrm{L}}-n_{\mathrm{C}})kT\left[\frac{\sum x_{is}\ln(x_{is}/x_{ia})}{x_{\mathrm{As}}}-\beta\frac{(\phi_{\mathrm{As}}-\phi_{\mathrm{Aa}})^2}{\phi_{\mathrm{As}}}\right]\\ &+N_{\mathrm{A}}kT\left[\frac{\sum x_{i0}\ln(x_{ia}/x_{i0})}{x_{\mathrm{A0}}}+\beta\frac{(\phi_{\mathrm{Aa}}-\phi_{\mathrm{A0}})^2}{\phi_{\mathrm{A0}}}\right],\end{aligned} \tag{14}$$

$$\text{with } \beta = Z_{\mathrm{v}}\left\{\varepsilon^*_{\mathrm{AA}}+\left(\frac{\sigma_{\mathrm{AA}}}{\sigma_{\mathrm{BB}}}\right)^3\varepsilon^*_{\mathrm{BB}}-2\left(\frac{\sigma_{\mathrm{AA}}}{\sigma_{\mathrm{AB}}}\right)^3\varepsilon^*_{\mathrm{AB}}\right\}-\left\{1+\left(\frac{\sigma_{\mathrm{AA}}}{\sigma_{\mathrm{BB}}}\right)^3-2\left(\frac{\sigma_{\mathrm{AA}}}{\sigma_{\mathrm{AB}}}\right)^3\right\},$$

$$r=\left(\frac{\sigma_{\mathrm{BB}}}{\sigma_{\mathrm{AA}}}\right)^3,\ \phi_{\mathrm{A}}=\frac{x_{\mathrm{A}}}{x_{\mathrm{A}}+rx_{\mathrm{B}}},\ \phi_{\mathrm{B}}=\frac{rx_{\mathrm{B}}}{x_{\mathrm{A}}+rx_{\mathrm{B}}},$$

where T_{mb} is the freezing point of the solute, and Z_{m} and Z_{v} are the fusion and evaporation enthalpies of the LJ molecules, respectively, reduced by ε. The first and second terms in Eq. (14) represent stabilization by the formation of cores and shells, respectively, and the third one represents the finite size effect. The contributions of the interaction strength ε are summarized in the interaction parameter β. With respect to ΔG_S, we developed a simple estimation formula for interfacial tension (see supplemental material) inspired by the model proposed by Good and Elbing.[41] The interfacial tension of phases I and II, with solute compositions x_{AI} and $x_{\mathrm{AII}}(x_{\mathrm{AI}} \geq x_{\mathrm{AII}})$, is given as follows:

$$\gamma_{\mathrm{I,II}} = \gamma_{\mathrm{I}} + \gamma_{\mathrm{II}} - 2C_{\mathrm{I,II}}(\gamma_{\mathrm{I}}\gamma_{\mathrm{II}})^{\frac{1}{2}}, \tag{15}$$

where γ_{I} and γ_{II} are the surface tensions of phases I and II, respectively, and $C_{\mathrm{I,II}}$ is the parameter related to the affinity of the two phases. $C_{\mathrm{I,II}}$ and surface tension of a phase with solute composition x_{A} can be calculated using the following equations:

$$\gamma(x_{\mathrm{A}}) = \kappa_j\frac{kT\left(\varepsilon^*_{\mathrm{AA}}{\phi_{\mathrm{A}}}^2+2\varepsilon^*_{\mathrm{AB}}\phi_{\mathrm{A}}\phi_{\mathrm{B}}+\varepsilon^*_{\mathrm{BB}}{\phi_{\mathrm{B}}}^2\right)}{{\sigma_{\mathrm{AA}}}^2x_{\mathrm{A}}+{\sigma_{\mathrm{BB}}}^2x_{\mathrm{B}}}, \tag{16}$$

$$C_{\mathrm{I,II}} = 1-\left(1-\frac{\varepsilon^*_{\mathrm{AB}}}{\sqrt{\varepsilon^*_{\mathrm{AA}}\varepsilon^*_{\mathrm{BB}}}}\right)(X_{\mathrm{AI}}-X_{\mathrm{AII}}), \tag{17}$$

$$\text{where}\quad X_{\mathrm{A}}=\frac{{\sigma_{\mathrm{AA}}}^2x_{\mathrm{A}}}{{\sigma_{\mathrm{AA}}}^2x_{\mathrm{A}}+{\sigma_{\mathrm{BB}}}^2x_{\mathrm{B}}},$$

and κ_j is a coefficient that depends on the phase ($j = \mathrm{C}, \mathrm{L}$, C: crystal phase, L: liquid phase). Each parameter in Eqs. (13)–(17) is determined as follows: based on the equilibrium data of the LJ molecule obtained by Hansen and Verlet,[42] we set $Z_{\mathrm{m}} = 1.31$, $Z_{\mathrm{v}} = 6.62$, $v_{\mathrm{L}} = 1.143{\sigma_{\mathrm{AA}}}^3$, and $v_{\mathrm{C}} = 1.028{\sigma_{\mathrm{AA}}}^3$. These values correspond to $T^* = kT/\varepsilon = 0.75$, which is the closest to the temperature range of our simulations for Hansen and Verlet's data. The freezing point of the solute T_{mb} was set to $0.68\varepsilon_{\mathrm{AA}}/k$, which is valid except in the high-pressure region. For κ_j, a series of simulations and subsequent CNT-based analyses were conducted and $\kappa_{\mathrm{L}} = 1.72$ and $\kappa_{\mathrm{C}} = 3.62$ were calculated (See supplemental material). In the above settings, the temperature dependence of the parameters was not considered.

Pathway prediction based on free energy profile

We first assumed a simplified case in which the contribution of the proximity of two interfaces is negligible ($\Psi = 0$). Figure 5 shows free energy profiles on an n_{L}–n_{C} plane calculated based on our proposed model. In these profiles, the lower left region near the origin $(n_{\mathrm{L}}, n_{\mathrm{C}}) = (0,0)$ corresponds to the solution state, the lower right area with large n_{L} and small n_{C} corresponds to the liquid cluster, and the upper right area where both n_{L} and n_{C} are large corresponds to the crystal. In the free energy profile for the typical condition of $(\varepsilon^*_{\mathrm{AA}}, \Delta\varepsilon^*) = (2.0, 0.67)$, where a two-step nucleation is observed in the MD simulation (Fig. 2a), the global minimum existed at $(n_{\mathrm{L}}, n_{\mathrm{C}}) = (1100,1100)$, which corresponds to the crystal state (Fig. 5a). According to the profile, the system will not follow a direct pathway along the $n_{\mathrm{L}} = n_{\mathrm{C}}$ line from the initial solution to the stable crystal state because of an energy barrier between the two states. Instead, it will take a "roundabout" path via a local minimum of the liquid cluster state at (1000,0) to the stable crystal state, thereby circumventing the peak height of the energy barrier. This demonstrates that a two-step nucleation, which corresponds to the ripening regime.[43], is more favorable under the typical condition. In the profile for the condition of $(\varepsilon^*_{\mathrm{AA}}, \Delta\varepsilon^*) = (2.67, 0.60)$, where the one-step nucleation is observed in MD simulation (Fig. 2b), the energy barrier is located close to the n_{L} axis. Hence, it prevents the liquid cluster formation (Fig. 5b). Therefore, the system would follow the pathway along the $n_{\mathrm{L}} = n_{\mathrm{C}}$ line with a lower energy barrier than that of the liquid cluster formation, making a one-step nucleation energetically preferable. The peak location and height of the energy barrier thus determine the nucleation behavior so that a pathway with lower barrier is selected. For both conditions, the calculated free energy profiles demonstrated that the transition from the initial solution state involved an activation process to overcome an energy barrier and accordingly required an induction time.

In contrast to the above two conditions involving the activation processes from the metastable initial solution state, the region near the origin $(n_{\mathrm{L}}, n_{\mathrm{C}}) = (0,0)$ is unstable under the two conditions of $\Delta\varepsilon^* = 1.34$ as shown in Figs. 5c and 5d. This accounts for the spontaneous solute assembly forming liquid clusters without induction times, as observed in Figs. 2c and 2d. The difference in the pathways in Figs. 2c and 2d can be explained by the difference in the critical size (energy barrier height) in the n_{C} axis direction. In Figs. 5c and 5d, ridges in the free energy profiles lying between the regions of small and large n_{C} values are indicated by dotted lines. The ridges correspond to the critical crystal size n^*_{C} for the crystallization of an n_{L}-size liquid cluster. The critical size n^*_{C} in Fig. 5c is approximately twice as large as that in Fig. 5d,

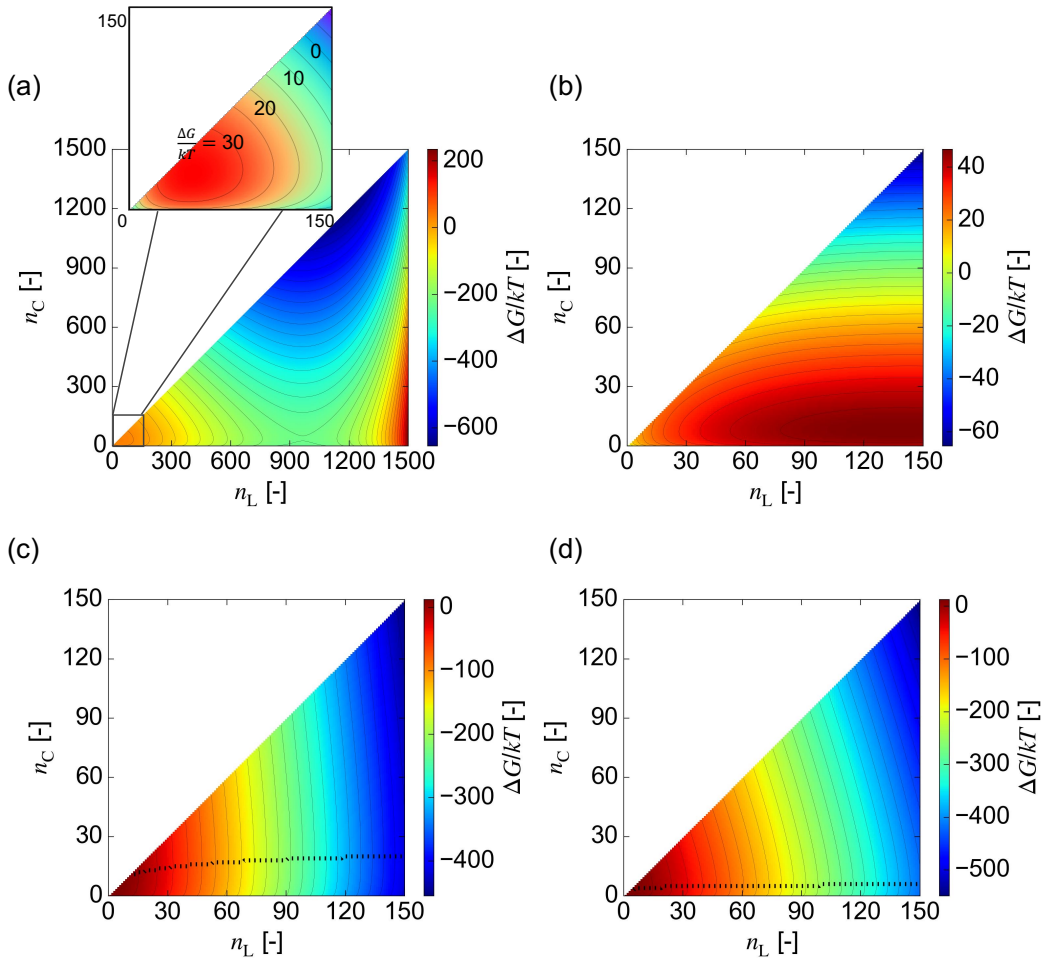

Fig. 5. Free energy profiles on the n_L–n_C plane calculated via our proposed model for different conditions of (a) $(\varepsilon^*_{AA}, \Delta\varepsilon^*) = (2.0, 0.67)$, (b) $(\varepsilon^*_{AA}, \Delta\varepsilon^*) = (2.67, 0.60)$, (c) $(\varepsilon^*_{AA}, \Delta\varepsilon^*) = (2.0, 1.34)$, and (d) $(\varepsilon^*_{AA}, \Delta\varepsilon^*) = (2.67, 1.34)$. The parameter sets of (a)–(d) correspond to those of Figs. 2(a)–(d), respectively. Black dotted lines in figures (c) and (d) indicate the critical crystal size n^*_C for the crystallization of n_L-size liquid clusters.

which qualitatively accounts for the slow crystallization in Fig. 2c and instantaneous crystallization in Fig. 2d.

In this way, the free energy profiles calculated by our proposed model are consistent with all four different nucleation behaviors observed in the MD simulations, demonstrating the validity and applicability of the core-shell CNT model to molecular systems. The key parameters that determine the nucleation behavior are determined to be ε^*_{AA} and $\Delta\varepsilon^*$. The roles of the two parameters in the free energy calculation become clearer when we deform Eq. (18) into Eq. (14) by assuming that the solute and solvent sizes are equal, the change in the solution concentration owing to nucleation is small, and the solvent fraction of the liquid cluster is negligible:

$$\Delta G_V \approx n_C kT\left[\ln x_{As} - Z_m \varepsilon^*_{AA}\left(\frac{T_{mb}-T}{T_{mb}}\right)\right] + n_L kT\left[\ln\frac{x_{As}}{x_{A0}} - Z_v\,\Delta\varepsilon^*\frac{(x_{As}-x_{A0})^2}{x_{As}}\right]. \quad (18)$$

The first and second terms represent the stabilization due to the formation of crystalline cores and solute assembly, respectively. The first term depends on the temperature difference $T_{mb} - T$, which can be interpreted as the supercooling of the liquid cluster, whereas the second term is governed by the composition (concentration) difference $x_{As} - x_{A0}$ which corresponds to the supersaturation of the solution phase. The molecular interaction parameters ε^*_{AA} and $\Delta\varepsilon^*$ appear as coefficients of the temperature difference $T_{mb} - T$ and the composition difference $x_{As} - x_{A0}$, respectively. Therefore, the parameters ε^*_{AA} and $\Delta\varepsilon^*$ define the degree of supercooling and supersaturation, respectively, and the balance between the two parameters determines the peak position of the energy barrier in the free energy profiles and, accordingly, the nucleation pathway.

Effect of the interaction between the two interfaces

Although the possible pathways drawn from the calculated free energy profiles qualitatively agree with the simulation results, the proposed core-shell CNT model still has room for improvement toward the quantitative prediction of the nucleation pathway. A missing piece in our model is the interfacial effect at the nanoscale because we assumed $\Psi = 0$ in the previous section. Accordingly, we introduced the freezing point depression of the liquid clusters caused by the Gibbs-Thomson effect[44] into our model by replacing T_{mb} in Eq.

(10) with the freezing point T_m of a liquid cluster with n_L solute molecules, where T_m is expressed as (See supplemental material):

$$T_m = T_{mb}\left(1 - \frac{2\gamma_C a_C^{\frac{2}{3}}}{3kTZ_m\varepsilon_{AA}^* n_L^{\frac{1}{3}}}\right). \quad (19)$$

The introduction of freezing point depression corresponds to the manipulation of Ψ because Ψ reflects the penalty of crystallization within the confined space of a liquid cluster. Figure 6a shows the free energy profile calculated with the modified model for the typical condition of $(\varepsilon_{AA}^*, \Delta\varepsilon^*) = (2.0, 0.67)$. The general trend is similar to that shown in Fig. 5a, in which the initial solution and liquid cluster states are metastable and the crystal state is the most stable. However, a critical difference is noticed with the height and location of the energy barrier. Compared with Fig. 5a, the energy barrier is higher and located closer to the $n_L = n_C$ line in Fig. 6a, which reflects the lower stability of smaller nuclei due to the Gibbs-Thomson effect. As a result, liquid cluster formation followed by its crystallization is more plausible in Fig. 6a than that in Fig. 5a because of the lower energy barrier for the pathway along the n_L axis. Consequently, the calculated profile successfully describes the pathway observed in the MD simulation (solid black line in Fig. 6a). The modified model also improves the calculated profile for the condition of $(\varepsilon_{AA}^*, \Delta\varepsilon^*) = (2.67, 0.60)$. In the profile from the original model (Fig. 5b), the energy barrier is located along the n_L axis to deny a two-step pathway. In contrast, in the modified profile (Fig. 6b), the peak of the energy barrier is shifted closer to the $n_L = n_C$ line, which lowers the height of the energy barrier for liquid cluster formation compared to that for crystal formation. In fact, a close look at Fig. 2b clarifies that the liquid cluster formation precedes the crystallization by several nanoseconds (Fig. 2b and the solid black line in Fig. 6b), which is accounted for in terms of the calculated profile (Fig. 6b). In addition, the modified model can more quantitatively describe the pathways of Figs. 2c and 2d under the conditions of $\Delta\varepsilon^* = 1.34$ than the original model. As shown in Figs. 6c and 6d, the critical size n_C^* of n_L-size liquid clusters (dotted lines in Fig. 6c and 6d) become larger than those of the original model (Fig. 5c and 5d) due to the Gibbs-Thomson effect. This trend is pronounced in the profile of Fig.

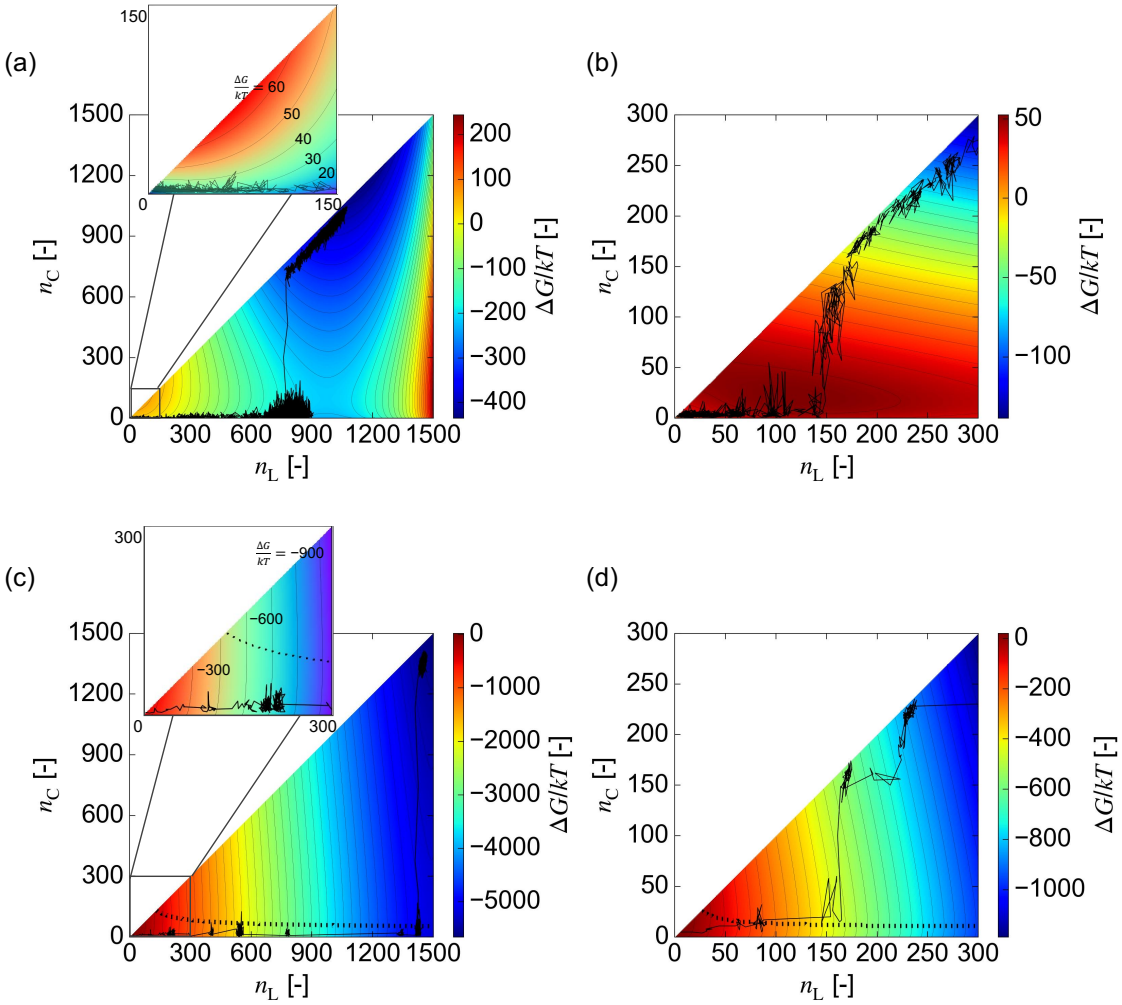

Fig. 6. Free energy profiles on an n_L–n_C plane calculated via the modified model for parameter sets of (a) $(\varepsilon_{AA}^*, \Delta\varepsilon^*) = (2.0, 0.67)$, (b) $(\varepsilon_{AA}^*, \Delta\varepsilon^*) = (2.67, 0.60)$, (c) $(\varepsilon_{AA}^*, \Delta\varepsilon^*) = (2.0, 1.34)$, and (d) $(\varepsilon_{AA}^*, \Delta\varepsilon^*) = (2.67, 1.34)$. The parameter sets of (a)–(d) correspond to those of Figs. 2(a)–(d), respectively. Black solid lines indicate typical observed pathways for each parameter set. Black dotted lines in figure (c) and (d) indicate the critical crystal size n_C^* for the crystallization of n_L-size liquid clusters.

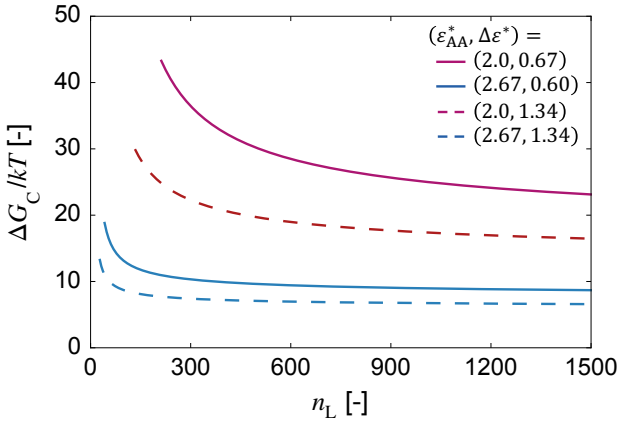

Fig. 7. Energy barrier for the crystallization of an n_L-size liquid cluster, ΔG_C^*, for parameter sets of $(\varepsilon_{AA}^*, \Delta\varepsilon^*) = (2.0, 0.67)$, $(2.67, 0.60)$, $(2.0, 1.34)$, and $(2.67, 1.34)$. These parameter sets correspond to those of Figs. 2(a)–(d), respectively.

6c while limited in Fig. 6d, which are consistent with the difference in the timing of crystallization (solid black lines in Fig. 6c and 6d).

In all the four cases, the system is driven to first form liquid clusters, because a small crystal is unstable and the timing of the crystallization defines the nucleation behavior. Figure 7 shows the energy barrier for the crystallization of an n_L-size liquid cluster, ΔG_C^*, under the four conditions. The height of the crystallization barrier decreases with n_L because the Gibbs-Thomson effect diminishes through the growth of liquid clusters. Under the conditions of $\varepsilon_{AA}^* = 2.0$, where the degree of supercooling in bulk is small, the barrier for the crystallization is high, and the crystallization rarely occurs until liquid clusters grow into the size close to the local minimum, which results in a certain induction time for the crystallization (Figs. 2a, 2c and 6a, 6c). In contrast, under the conditions of $\varepsilon_{AA}^* = 2.67$, where the degree of supercooling in the bulk is large, the crystallization barrier is sufficiently low even for small n_L values. Hence, crystallization occurs as soon as the liquid clusters reach a certain size, which is much smaller than that at the local minimum, leading to an instantaneous crystallization (Figs. 2b, 2d and 6b, 6d). Based on these results, it can be concluded that the nucleation pathway is essentially a two-step pathway. Moreover, as the degree of supercooling increases, the pathway asymptotically approaches one-step behavior.

The agreement between the observed pathways and the free energy profiles described here supports the validity of the core-shell model in describing two-step nucleation, as confirmed in previous studies using lattice model[22] and NaCl systems,[33] although our model differs from them in the treatment of the proximity of the two interfaces. The model of the previous studies[22,31,33] directly describes the two interfaces proximity by introducing a parameter ξ expressing the range of the interfacial interaction, whereas our model incorporates the interfaces proximity through the Gibbs-Thomson effect, which is a somewhat indirect approach. However, our approach is more practical because the required parameters can be determined experimentally. Moreover, our model gives a relationship between microscopic molecular interactions and macroscopic experimental parameters (degree of supersaturation and degree of supercooling), which offers applicability to experimental systems. Although other influencing factors, such as charge and molecular shape, need to be taken into account when dealing with real molecules, we believe that our model provides a basis for predicting pathways based on molecular properties.

Conclusion

In this study, we investigated the nucleation processes in a binary LJ system as a model system for molecular solutions to clearly determine the key factors governing the nucleation pathway. We conducted MD simulations in the *NPT* ensemble with various interaction strengths, and found that the nucleation behaviors can be classified into four types: (1) two-step nucleation with induction times for both liquid-cluster formation and crystallization, (2) one-step nucleation characterized by simultaneous solute assembly and crystallization with an induction time, (3) two-step nucleation with the quick assembly of solutes and slow crystallization, and (4) one-step nucleation characterized by instantaneous liquid cluster formation and crystallization. The quick assembly of solutes occurs at a higher value of $\Delta\varepsilon^* = \varepsilon_{AA}^* + \varepsilon_{BB}^* - 2\varepsilon_{AB}^*$ (the difference between the strength of like-pair interactions and that of unlike-pair interactions), whereas the instantaneous crystallization of liquid clusters stems from a higher value of ε_{AA}^* (the strength of solute-solute interaction). All four nucleation behaviors were accounted for by the combination of $\Delta\varepsilon^*$ and ε_{AA}^*, indicating that these two interaction parameters are the determining factors for the nucleation behavior. We theoretically confirmed this finding by extending the core-shell CNT model to a solution system with a finite system size. The free energy profiles calculated by our proposed model are qualitatively consistent with all four different nucleation behaviors observed in the MD simulations, demonstrating the validity and applicability of the core-shell CNT model to molecular systems. Our model demonstrates that the parameters ε_{AA}^* and $\Delta\varepsilon^*$ define the degree of supercooling and supersaturation, respectively. In addition, the balance between the two parameters determines the peak position of the energy barrier in the free energy profiles and, accordingly, the nucleation pathway. Furthermore, we considered the interfacial effect at the nanoscale in our model to be the freezing point depression of liquid clusters caused by the Gibbs-Thomson effect. The modified model more precisely describes the observed pathway. It indicates that the nucleation pathway is essentially a two-step pathway; as the degree of supercooling increases, the pathway asymptotically approaches one-step behavior. Thus, our model is a milestone in predicting and controlling the nucleation pathways of simple systems. It is worth noting that the molecular properties and operating conditions were the only parameters used in our model to calculate the free energy changes through nucleation. Because molecular properties can be represented by interaction and size parameters, we believe that our model is applicable to more complex molecules to describe the nucleation behavior through their physical properties.

Figure captions.

Fig. 1. Snapshots from MD simulation for a parameter set of $(\varepsilon^*_{AA}, \varepsilon^*_{BB}, \varepsilon^*_{AB}) = (2.0, 1.34, 1.34)$, in which only solute molecules are shown for clarity. The lower right insets of states (II) and (III) are the cross-sectional views of the assembled structures.

Fig. 2. Time courses of n_L and n_C for four parameter sets of (a) $(\varepsilon^*_{AA}, \varepsilon^*_{BB}, \varepsilon^*_{AB}) = (2.0, 1.34, 1.34)$, $\Delta\varepsilon^* = 0.67$, (b) $(\varepsilon^*_{AA}, \varepsilon^*_{BB}, \varepsilon^*_{AB}) = (2.67, 1.34, 1.70)$, $\Delta\varepsilon^* = 0.60$, (c) $(\varepsilon^*_{AA}, \varepsilon^*_{BB}, \varepsilon^*_{AB}) = (2.0, 1.34, 1.0)$, $\Delta\varepsilon^* = 1.34$, and (d) $(\varepsilon^*_{AA}, \varepsilon^*_{BB}, \varepsilon^*_{AB}) = (2.67, 1.34, 1.34)$, $\Delta\varepsilon^* = 1.34$. In figure (a), time zones I, II, and III correspond to solution state (I), liquid cluster (II), and crystal (III) of Fig. 1, respectively.

Fig. 3. Average induction time for liquid cluster formation τ_L and mean cluster size n_L at crystallization for various parameter sets. The simulations for the parameter sets of $(\varepsilon^*_{AA}, \varepsilon^*_{BB}, \varepsilon^*_{AB}) = (2.0, 1.0, 1.17)$ and $(2.0, 1.0, 0.83)$ were conducted at 240 K.

Fig. 4. Schematic of the proposed model

Fig. 5. Free energy profiles on the n_L–n_C plane calculated via our proposed model for different conditions of (a) $(\varepsilon^*_{AA}, \Delta\varepsilon^*) = (2.0, 0.67)$, (b) $(\varepsilon^*_{AA}, \Delta\varepsilon^*) = (2.67, 0.60)$, (c) $(\varepsilon^*_{AA}, \Delta\varepsilon^*) = (2.0, 1.34)$, and (d) $(\varepsilon^*_{AA}, \Delta\varepsilon^*) = (2.67, 1.34)$. The parameter sets of (a)–(d) correspond to those of Figs. 2(a)–(d), respectively. Black dotted lines in figures (c) and (d) indicate the critical crystal size n^*_C for the crystallization of n_L-size liquid clusters.

Fig. 6. Free energy profiles on an n_L–n_C plane calculated via the modified model for parameter sets of (a) $(\varepsilon^*_{AA}, \Delta\varepsilon^*) = (2.0, 0.67)$, (b) $(\varepsilon^*_{AA}, \Delta\varepsilon^*) = (2.67, 0.60)$, (c) $(\varepsilon^*_{AA}, \Delta\varepsilon^*) = (2.0, 1.34)$, and (d) $(\varepsilon^*_{AA}, \Delta\varepsilon^*) = (2.67, 1.34)$. The parameter sets of (a)–(d) correspond to those of Figs. 2(a)–(d), respectively. Black solid lines indicate typical observed pathways for each parameter set. Black dotted lines in figure (c) and (d) indicate the critical crystal size n^*_C for the crystallization of n_L-size liquid clusters.

Fig. 7. Energy barrier for the crystallization of an n_L-size liquid cluster, ΔG^*_C , for parameter sets of $(\varepsilon^*_{AA}, \Delta\varepsilon^*) = (2.0, 0.67)$, $(2.67, 0.60)$, $(2.0, 1.34)$, and $(2.67, 1.34)$. These parameter sets correspond to those of Figs. 2(a)–(d), respectively.

ASSOCIATED CONTENT

Supporting Information.
The Supporting Information is available free of charge.
Additional explanation and Figures S1–S5 (PDF).

AUTHOR INFORMATION

Corresponding Author

*nabe@cheme.kyoto-u.ac.jp

Author Contributions

YI conducted the simulations and analyses and wrote the manuscript. TH and MM provided the instructions as supervisors. SW designed and supervised the research project and wrote the manuscript.

Notes
The authors declare no competing financial interest

ACKNOWLEDGMENT

This work was partially supported by the JSPS Grant-in-Aid for Scientific Research (B) (No. 20H02504) and the Grant-in-Aid for JSPS Fellows (No. 21J23476).

REFERENCES

(1) Rajh, T.; Mićić, O. I.; Nozik, A. J. Synthesis and Characterization of Surface-Modified Colloidal CdTe Quantum Dots. *J. Phys. Chem.* **1993**, *97*, 11999–12003.

(2) Lee, E. H. A Practical Guide to Pharmaceutical Polymorph Screening & Selection. *Asian J. Pharm. Sci.* **2014**, *9*, 163–175.

(3) Gibbs, J. W. On the Equilibrium of Heterogeneous Substances. *Trans. Connect. Acad. Arts Sci.* **1876**, *3*, 108–248.

(4) Volmer, M.; Weber, A. Keimbildung in Übersättigten Gebilden. *Z. Phys. Chem.* **1926**, *119*, 277–301.

(5) Becker, R.; Döring, W. Kinetische Behandlung Der Keimbildung in Übersättigten Dämpfen. *Ann. Phys.* **1935**, *24*, 719–752.

(6) Zeldvich, J. B. On the Theory of New Phase Formation. Cavitation. *Acta Physicochim. URSS* **1943**, *18*, 1–22.

(7) Sinha, S.; Bhabhe, A.; Laksmono, H.; Wölk, J.; Strey, R.; Wyslouzil, B. Argon Nucleation in a Cryogenic Supersonic Nozzle. *J. Chem. Phys.* **2010**, *132*, 064304.

(8) Tanaka, K. K.; Tanaka, H.; Yamamoto, T.; Kawamura, K. Molecular Dynamics Simulations of Nucleation from Vapor to Solid Composed of Lennard-Jones Molecules. *J. Chem. Phys.* **2011**, *134*, 204313.

(9) Dillmann, A.; Meier, G. E. A. A Refined Droplet Approach to the Problem of Homogeneous Nucleation from the Vapor Phase. *J. Chem. Phys.* **1991**, *94*, 3872.

(10) Vekilov, P. G. Nucleation. *Cryst. Growth Des.* **2010**, *10*, 5007–5019.

(11) Loh, N. D.; Sen, S.; Bosman, M.; Tan, S. F.; Zhong, J.; Nijhuis, C. A.; Král, P.; Matsudaira, P.; Mirsaidov, U. Multistep Nucleation of Nanocrystals in Aqueous Solution. *Nat. Chem.* **2017**, *9*, 77–82.

(12) Gebauer, D.; Völkel, A.; Cölfen, H. Stable Prenucleation Calcium Carbonate Clusters. *Science* **2008**, *322*, 1819–1822.

(13) Gebauer, D.; Kellermeier, M.; Gale, J. D.; Bergström, L.; Cölfen, H. Pre-Nucleation Clusters as Solute Precursors in Crystallisation. *Chem. Soc. Rev.* **2014**, *43*, 2348–2371.

(14) Penn, R. L.; Banfield, J. F. Imperfect Oriented Attachment: Dislocation Generation in Defect-Free Nanocrystals. *Science* **1998**, *281*, 969–971.

(15) Vekilov, P. G. The Two-Step Mechanism of Nucleation of Crystals in Solution. *Nanoscale* **2010**, *2*, 2346–2357.

(16) Zhang, T. H.; Liu, X. Y. Multistep Crystal Nucleation: A Kinetic Study Based on Colloidal Crystallization. *J. Phys. Chem. B* **2007**, *111*, 14001–14005.

(17) Salvalaglio, M.; Perego, C.; Giberti, F.; Mazzotti, M.; Parrinello, M. Molecular-Dynamics Simulations of Urea Nucleation from Aqueous Solution. *Proc. Natl. Acad. Sci. U. S. A.* **2015**, *112*, E6–E14.

(18) Jiang, H.; Debenedetti, P. G.; Panagiotopoulos, A. Z. Nucleation in Aqueous NaCl Solutions Shifts from 1-Step to 2-Step Mechanism on Crossing the Spinodal. *J. Chem. Phys.* **2019**, *150*, 124502.

(19) Finney, A. R.; Salvalaglio, M. Multiple Pathways in NaCl Homogeneous Crystal Nucleation. *Faraday Discuss.* **2021**, *235*, 56–80.

(20) Salvalaglio, M.; Mazzotti, M.; Parrinello, M. Urea Homogeneous Nucleation Mechanism Is Solvent Dependent. *Faraday Discuss.* **2015**, *179*, 291–307.

(21) Duff, N.; Peters, B. Nucleation in a Potts Lattice Gas Model of Crystallization from Solution. *J. Chem. Phys.* **2009**, *131*, 184101.

(22) Eaton, D.; Saika-Voivod, I.; Bowles, R. K.; Poole, P. H. Free Energy Surface of Two-Step Nucleation. *J. Chem. Phys.* **2021**, *154*, 234507.

(23) Hedges, L. O.; Whitelam, S. Limit of Validity of Ostwalds Rule of Stages in a Statistical Mechanical Model of Crystallization. *J. Chem. Phys.* **2011**, *135*, 164902.

(24) Frenkel, D.; Auer, S. Prediction of Absolute Crystal-Nucleation Rate in Hard-Sphere Colloids. *Nature* **2001**, *409*, 1020–1023.

(25) Punnathanam, S.; Monson, P. A. Crystal Nucleation in Binary Hard Sphere Mixtures: A Monte Carlo Simulation Study. *J. Chem. Phys.* **2006**, *125*, 024508.

(26) Van Meel, J. A.; Page, A. J.; Sear, R. P.; Frenkel, D. Two-Step Vapor-Crystal Nucleation Close below Triple Point. *J. Chem. Phys.* **2008**, *129*, 204505.

(27) Chen, B.; Kim, H.; Keasler, S. J.; Nellas, R. B. An Aggregation-Volume-Bias Monte Carlo Investigation on the Condensation of a Lennard-Jones Vapor Below the Triple Point and Crystal Nucleation in Cluster Systems: An in-Depth Evaluation of the Classical Nucleation Theory. *J. Phys. Chem. B* **2008**, *112*, 4067–4078.

(28) Desgranges, C.; Delhommelle, J. Controlling Polymorphism during the Crystallization of an Atomic Fluid. *Phys. Rev. Lett.* **2007**, *98*, 235502.

(29) Ten Wolde, P. R.; Frenkel, D. Enhancement of Protein Crystal Nucleation by Critical Density Fluctuations. *Science* **1997**, *277*, 1975–1978.

(30) Whitelam, S. Control of Pathways and Yields of Protein Crystallization through the Interplay of Nonspecific and Specific Attractions. *Phys. Rev. Lett.* **2010**, *105*, 088102.

(31) Iwamatsu, M. Free-Energy Landscape of Nucleation with an Intermediate Metastable Phase Studied Using Capillarity Approximation. *J. Chem. Phys.* **2011**, *134*, 164508.

(32) Kashchiev, D. Classical Nucleation Theory Approach to Two-Step Nucleation of Crystals. *J. Cryst. Growth* **2020**, *530*, 125300.

(33) Bulutoglu, P. S.; Wang, S.; Boukerche, M.; Nere, N. K.; Corti, D. S.; Ramkrishna, D. An Investigation of the Kinetics and Thermodynamics of NaCl Nucleation through Composite Clusters. *PNAS Nexus* **2022**, *1*, 1–11.

(34) Desgranges, C.; Delhommelle, J. Free Energy Calculations along Entropic Pathways. II. Droplet Nucleation in Binary Mixtures. *J. Chem. Phys.* **2016**, *145*, 234505.

(35) Chen, B.; Siepmann, J. I.; Klein, M. L. Simulating the Nucleation of Water/Ethanol and Water/n-Nonane Mixtures: Mutual Enhancement and Two-Pathway Mechanism. *J. Am. Chem. Soc.* **2003**, *125*, 3113–3118.

(36) Zimmermann, N. E. R.; Vorselaars, B.; Quigley, D.; Peters, B. Nucleation of NaCl from Aqueous Solution: Critical Sizes, Ion-Attachment Kinetics, and Rates. *J. Am. Chem. Soc.* **2015**, *137*, 13352–13361.

(37) Agrawal, R.; Kofke, D. A. Thermodynamic and Structural Properties of Model Systems at Solid-Fluid Coexistence II. Melting and Sublimation of the Lennard-Jones System. *Mol. Phys.* **1995**, *85*, 43–59.

(38) Bussi, G.; Donadio, D.; Parrinello, M. Canonical Sampling through Velocity Rescaling. *J. Chem. Phys.* **2007**, *126*, 014101.

(39) Parrinello, M.; Rahman, A. Polymorphic Transitions in Single Crystals: A New Molecular Dynamics Method. *J. Appl. Phys.* **1981**, *52*, 7182.

(40) Tribello, G. A.; Giberti, F.; Sosso, G. C.; Salvalaglio, M.; Parrinello, M. Analyzing and Driving Cluster Formation in Atomistic Simulations. *J. Chem. Theory Comput.* **2017**, *13*, 1317–1327.

(41) Good, R. J.; Elbing, E. R. J. Generalization of Theory for Estimation of Interfacial Energies. *Ind. Eng. Chem.* **1970**, *62*, 54–78.

(42) Hansen, J. P.; Verlet, L. Phase Transitions of the Lennard-Jones System. *Phys. Rev.* **1969**, *184*, 151.

(43) Agarwal, V.; Peters, B. Solute Precipitate Nucleation: A Review of Theory and Simulation Advances. *Adv. Chem. Phys.* **2014**, *155*, 97–160.

(44) Jackson, C. L.; McKenna, G. B. The Melting Behavior of Organic Materials Confined in Porous Solids. *J. Chem. Phys.* **1990**, *93*, 9002.

TOC Graphic

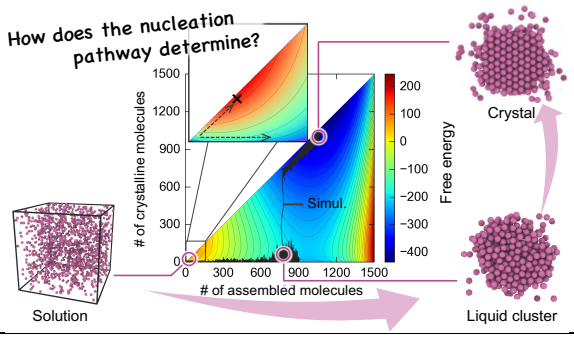
How does the nucleation pathway determine?
# of crystalline molecules
# of assembled molecules
Free energy
Simul.
Crystal
Solution
Liquid cluster